

# Spectroscopic signatures of magnetization-induced band renormalization and strong spin-charge-lattice coupling in $\text{EuZn}_2\text{As}_2$

Zhiyu Liao,<sup>1,2,\*</sup> Boxuan Li,<sup>1,2,\*</sup> Shaohui Yi,<sup>1,2</sup> Lincong Zheng,<sup>1</sup> Yubiao Wu,<sup>1</sup> Enkui Yi,<sup>3</sup> Premysl Marsik,<sup>4</sup> Bing Shen,<sup>3,†</sup> Hongming Weng,<sup>1,2,‡</sup> Bing Xu,<sup>1,2,§</sup> Xianggang Qiu,<sup>1,2</sup> and Christian Bernhard<sup>4</sup>

<sup>1</sup>*Beijing National Laboratory for Condensed Matter Physics, Institute of Physics, Chinese Academy of Sciences, P.O. Box 603, Beijing 100190, China*

<sup>2</sup>*School of Physical Sciences, University of Chinese Academy of Sciences, Beijing 100049, China*

<sup>3</sup>*State Key Laboratory of Optoelectronic Materials and Technologies,*

*School of Physics, Sun Yat-Sen University, Guangzhou, Guangdong 510275, China*

<sup>4</sup>*University of Fribourg, Department of Physics and Fribourg Center for Nanomaterials, Chemin du Musée 3, CH-1700 Fribourg, Switzerland*

We report an infrared spectroscopy study of the antiferromagnetic (AFM) insulator  $\text{EuZn}_2\text{As}_2$  over a broad frequency range, spanning temperatures both above and below the AFM transition  $T_N \simeq 20$  K. The optical response reveals an insulating behavior, featuring two prominent infrared-active phonon modes at around 95 and 190  $\text{cm}^{-1}$ , and two subtle absorption peaks at around 130 ( $\alpha$  peak) and 2700  $\text{cm}^{-1}$  ( $\beta$  peak), along with a strong absorption edge rising around 9000  $\text{cm}^{-1}$  ( $\gamma$  peak). Significantly, the temperature-dependent changes in these peaks show noticeable anomalies across the AFM transition, particularly the emergence of the  $\alpha$  peak and an unusual redshift of the  $\gamma$  peak, suggesting a strong interaction between the charge excitations and the AFM order. Band structure calculations reveal that these anomalies arise from magnetization-induced band renormalizations, including shifts and foldings. Additionally, both phonon modes feature asymmetric Fano line shapes at low temperatures, with the 95  $\text{cm}^{-1}$  phonon mode exhibiting strong coupling to the fluctuations of Eu spins. These findings highlight a complex interplay of spin, charge, and lattice degrees of freedom in  $\text{EuZn}_2\text{As}_2$ .

Recently, europium-based 122 pnictides  $\text{EuM}_2\text{X}_2$  ( $M = \text{Zn, In, Cd}$ ;  $X = \text{P, As, Sb}$ ) have attracted significant attention as promising candidates for intrinsic magnetic topological materials [1–4]. In these compounds, the interplay between the Eu-4*f* magnetic moment and the electronic band structure gives rise to a variety of fascinating quantum states, making these materials particularly intriguing for both fundamental research and potential spintronic applications. For instance, in  $\text{EuCd}_2\text{As}_2$  [5–9], the highly-tunable Eu moments can induce nontrivial topological phases, such as Dirac semimetal, Weyl semimetal, and higher-order topological insulator. In  $\text{EuIn}_2\text{As}_2$  and  $\text{EuSn}_2\text{As}_2$  [10, 11], the magnetic ground states play a key role in forming the axion insulator states, highlighting the importance of magnetic order in shaping the topological properties. Additionally, Eu-based pnictides are well-known for exhibiting colossal magnetoresistance effect [12–19]. Therefore, the strong spin-charge interaction in Eu-based materials can provide an ideal platform for manipulating band topology and exploring novel physical properties.

In contrast to the metallic hole-doped nature of the aforementioned several Eu-122 compounds, the newly discovered  $\text{EuZn}_2\text{As}_2$  exhibits an antiferromagnetic (AFM) insulator ground state with  $T_N \simeq 20$  K [20–23]. This compound has the same trigonal  $\text{CaAl}_2\text{Si}_2$ -type crystal structure (space group  $P\bar{3}m1$ , No. 164) and A-type AFM order as  $\text{EuCd}_2\text{As}_2$ . In this structure, the  $\text{Zn}_2\text{As}_2$  bilayers are separated by the triangular Eu layers, where the Eu local spins align ferromagnetically within the ab-plane and point along the

a/b-axis, while they order antiferromagnetically between adjacent Eu layers, as illustrated in the inset of Figure 1(a). Transport measurements in  $\text{EuZn}_2\text{As}_2$  have revealed dominant ferromagnetic fluctuations above  $T_N$  that result in an anomalous Hall effect and large negative magnetoresistance [23, 24]. First-principles calculations have predicted a topologically trivial insulator in the AFM phase, and a Weyl semimetal phase under ferromagnetic order [20, 24]. Quantum oscillation measurements have unveiled a complex hole band shape with nontrivial topological features [25]. Despite these intriguing findings, investigations into the underlying interplay between magnetism and the electronic degrees of freedom are scarce, particularly regarding how AFM order influences the topological properties and electronic structure of this material.

In this Letter, we present an infrared spectroscopy study to explore the electron and lattice dynamics in  $\text{EuZn}_2\text{As}_2$ . We examine the temperature-dependent optical response and, in particular, its changes at the onset of the magnetic order. Our optical results reveal that the AFM transition induces significant anomalies in both the charge and lattice excitations, providing valuable insights into the interplay between the charge, spin, and lattice degrees of freedom in this system. Additional band calculations show that the AFM order leads to a strong renormalization of the bands and a nearly closed bulk energy gap, placing  $\text{EuZn}_2\text{As}_2$  near a topological phase transition.

Sample synthesis, experimental methods, and details of the DFT calculations are provided in the Supplemental

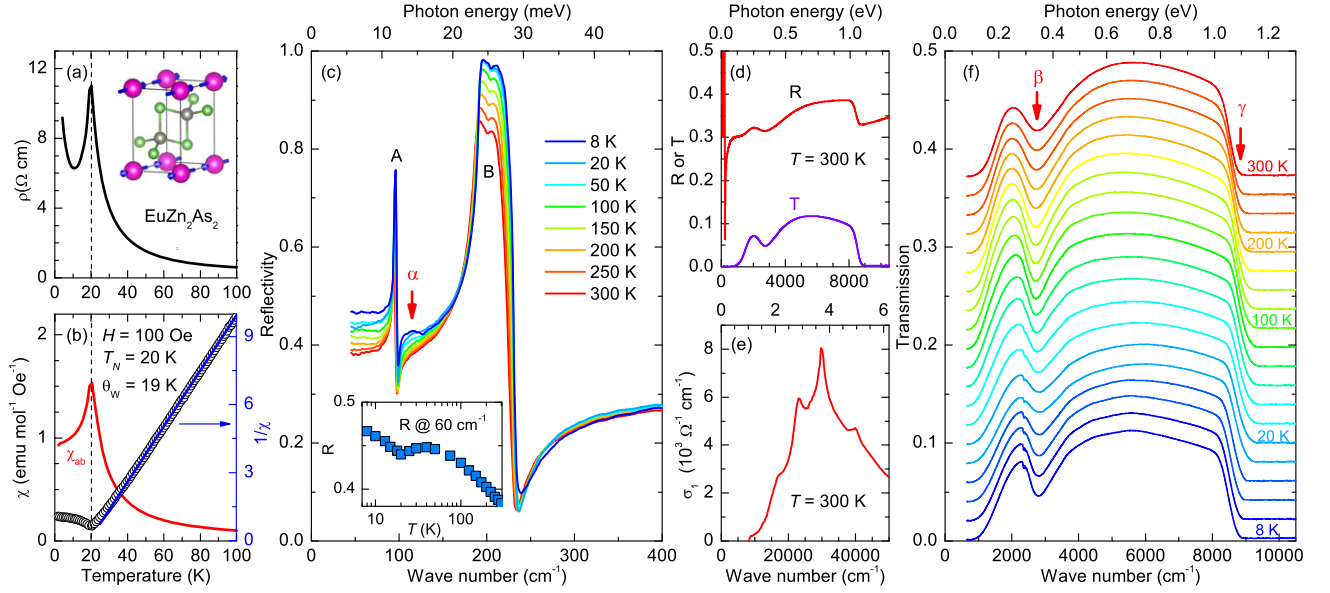


Figure 1. (a) Temperature-dependent resistivity  $\rho(T)$  with the current applied along the  $ab$ -plane for  $\text{EuZn}_2\text{As}_2$ . Inset shows the schematic crystal structure and magnetic configuration of Eu atoms. (b) Temperature dependence of magnetic susceptibility (red line, left axis) and the inverse of magnetic susceptibility (black circles, right axis). The magnetic field  $H$  is applied parallel to the  $ab$ -plane. Solid blue line is the fitting curve by the Curie-Weiss law. (c) Temperature-dependent in-plane reflectivity spectra of  $\text{EuZn}_2\text{As}_2$  in the far-infrared region. Inset: temperature-dependent reflectivity at  $60 \text{ cm}^{-1}$ . (d) The reflectivity and transmission spectra at  $300 \text{ K}$  up to  $10000 \text{ cm}^{-1}$ . (e) Optical conductivity spectrum measured by ellipsometry up to  $50000 \text{ cm}^{-1}$  at  $300 \text{ K}$ . (f) Temperature dependence of the in-plane transmission, with the data offset for clarity.

Materials [26].

Figure 1(a) displays the temperature ( $T$ ) dependence of the resistivity  $\rho(T)$  of  $\text{EuZn}_2\text{As}_2$ , which increases with decreasing  $T$ , suggesting a typical insulating behavior. In addition, a sharp resistivity peak around  $T_N = 20 \text{ K}$  coincides with a corresponding peak in the  $T$ -dependent magnetic susceptibility  $\chi(T)$ , shown in Figure 1(b). This feature is attributed to the AFM phase transition. Furthermore, the inverse susceptibility  $1/\chi$  above  $T_N$  is well described by the Curie-Weiss law  $\chi(T) = C/(T - \theta_W)$ , where  $\theta_W$  is the Weiss temperature and  $C$  is Curie constant. The positive value of  $\theta_W = 19 \text{ K}$  indicates the presence of dominant ferromagnetic correlations between the Eu ions, despite the AFM ground state. The deduced effective magnetic moment  $\mu_{\text{eff}} = 8.08 \mu_B$  ( $\mu_B$  is the Bohr magneton) is in close agreement with the theoretical value of  $7.94 \mu_B$  for the localized moment  $4f^7$ .

Figure 1(c) shows the in-plane reflectivity  $R(\omega)$  of  $\text{EuZn}_2\text{As}_2$  in the far-infrared region at several selected temperatures. The dominant features are two sharp peaks at  $95$  and  $190 \text{ cm}^{-1}$  (labeled as A and B), which are attributed to infrared-active phonons with  $E_u$  symmetry, reflecting the insulating nature of  $\text{EuZn}_2\text{As}_2$ . In addition, at low temperatures, a weak feature appears around  $130 \text{ cm}^{-1}$  (labeled as  $\alpha$ ), along with an increase in  $R(\omega)$  in the low-frequency limit. This temperature dependence is highlighted in the inset, where the increasing trend of  $R(\omega = 60 \text{ cm}^{-1})$  with decreasing  $T$  is interrupted by

the formation of a dip near  $T_N$ , indicating that the AFM order has a significant effect on the charge response.

In the high-frequency region, as shown in Fig.1(d), the reflectivity remains nearly constant, but exhibits a steplike drop around  $9000 \text{ cm}^{-1}$ , suggesting that the insulating sample is transparent. The transmittance measurements confirm this observation, since they show significant transmission between  $1000$  and  $9000 \text{ cm}^{-1}$ . The step feature around  $9000 \text{ cm}^{-1}$  corresponds to the absorption edge of the direct band gap. Furthermore, we obtained the optical conductivity at room temperature through ellipsometry measurements, as shown in Fig.1(e). It reveals an absorption onset around  $9000 \text{ cm}^{-1}$  (labeled as  $\gamma$ ), followed by a series of sharp peaks at  $17000$ ,  $23000$ ,  $30000$ , and  $40000 \text{ cm}^{-1}$ , which are attributed to high-energy interband transitions. To investigate the detailed  $T$  evolution of the insulating band gap, we measured transmission spectra at various temperatures, as shown in Fig. 1(f). In the mid-infrared region, the sample is transparent with a transmission of about 10%. A weak absorption feature exists around  $2700 \text{ cm}^{-1}$  (labeled as  $\beta$ ). In particular, as the temperature decreases, the absorption edge  $\gamma$  first shows a blueshift and then an anomalous redshift, indicating an anomalous change in the electronic structure.

In order to obtain the optical conductivity  $\sigma_1(\omega)$ , we fit the measured  $R(\omega)$  spectra at low energy using the Drude-Lorentz model. Details of the modeling are pro-

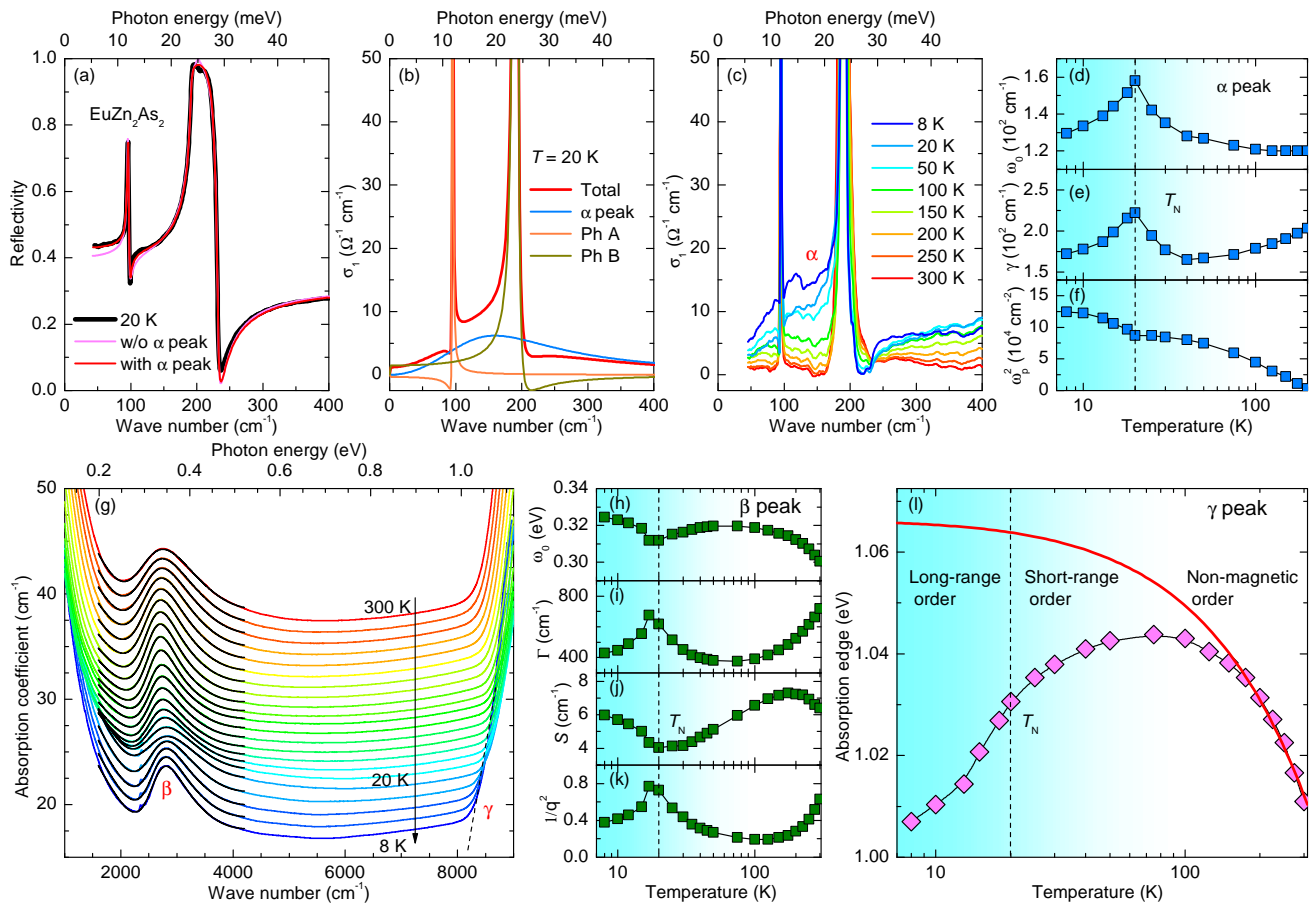


Figure 2. (a) Drude-Lorentz fitting of the reflectivity at 20 K. (b) Decomposition of the corresponding real part of the optical conductivity  $\sigma_1(\omega)$  at 20 K. (c) Temperature dependence of the  $\sigma_1(\omega)$  spectra obtained from Kramers-Kronig analysis of reflectivity in the far-infrared range. (d–f) Temperature dependence of the resonance frequency  $\omega_0$ , linewidth  $\gamma$ , and oscillator intensity  $\omega_p^2$  for  $\alpha$  peak. (g) Temperature dependence of the absorption coefficient. (h–k) Temperature dependence of the resonance frequency  $\omega_0$ , linewidth  $\gamma$ , and oscillator strength  $S$  and Fano parameter  $1/q^2$  for the  $\beta$  absorption peak. (l) Temperature dependence of the energy gap edge of  $\gamma$  peak.

vided in the Supplemental Materials [26]. Figure 2(a) displays the fitting results of  $R(\omega)$  at 20 K. Firstly, two Fano oscillators are used to fit the two phonon modes, where the measured  $R(\omega)$  can be almost reproduced, except for the  $\alpha$  peak feature and a lower reflectivity value in the zero-frequency limit. To improve the fit, an additional Lorentz oscillator is included to capture the  $\alpha$  peak feature. With this adjustment, the fitting result agrees much better with the measured  $R(\omega)$ . Figure 2(b) shows the corresponding optical conductivity, which consists of two phonon modes with asymmetric line shapes and the  $\alpha$  peak centered around  $130 \text{ cm}^{-1}$ . No Drude response appears in the  $\sigma_1(\omega)$  spectra, in line with our resistivity measurement. The  $\sigma_1(\omega)$  spectra are also derived via the Kramers-Kronig analysis of  $R(\omega)$  in the far-infrared range. As shown in Fig. 2(c),  $\sigma_1(\omega)$  near  $130 \text{ cm}^{-1}$  gradually enhances upon cooling, indicating the emergence of the  $\alpha$  component at low temperatures, in agreement with the modeled  $\sigma_1(\omega)$ . Figs. 2(d–f) display the tem-

perature dependence of the fitting parameters for the  $\alpha$  peak. The parameters  $\omega_0$ ,  $\gamma$ , and  $\omega_p$  all show distinct anomalies around  $T_N$ , demonstrating a strong interplay between the spin and charge degrees of freedom.

Next, we examine the  $T$ -evolution of the charge excitations in the high-energy region. Figure 2(g) shows the  $T$  dependence of the absorption coefficient,  $\alpha(\omega) = (1/d)\ln[1/t(\omega)]$ , where  $d = 1.3 \text{ mm}$  is the thickness of the sample and  $t(\omega)$  is the transmission spectrum. The absorption peak ( $\beta$ ) around  $2700 \text{ cm}^{-1}$  exhibits an asymmetric line shape. As indicated by the thin black line, this peak is fitted using a Fano line shape with a quadratic background,  $\alpha(\omega) = S \left[ \frac{q^2 + 2qz - 1}{q^2(1+z^2)} \right]$ , where  $z = (\omega - \omega_0)/\Gamma$ , and  $\omega_0$ ,  $\Gamma$  and  $S$  represent the frequency, linewidth, and strength of the peak, respectively. The asymmetric profile is determined by the Fano parameter  $1/q^2$ . The  $T$ -dependent fitting parameters are shown in Figs. 2(h–k), all of which display anomalies around  $T_N$ , signaling a close correlation between the charge ex-

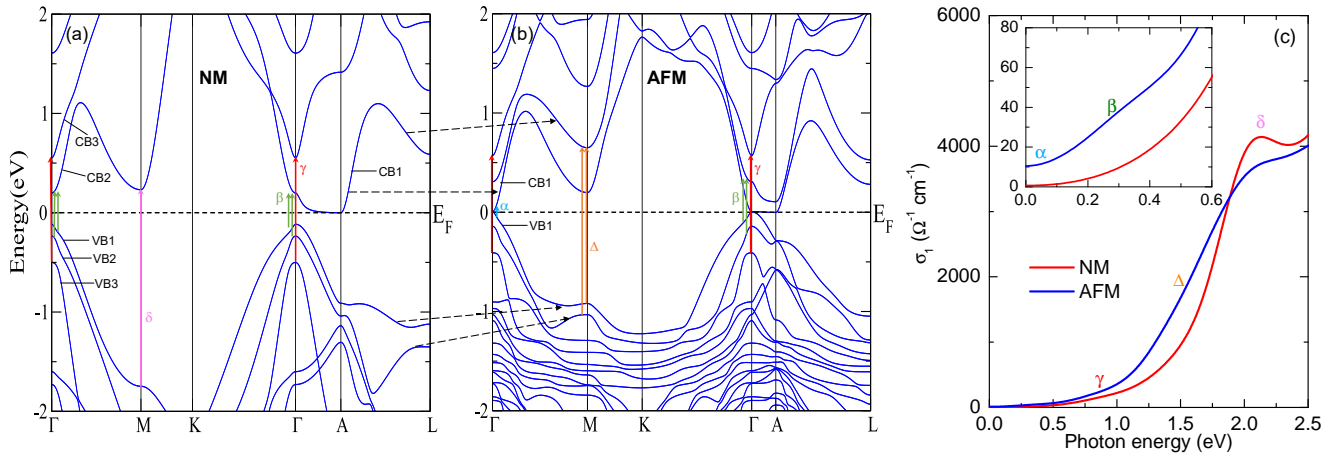


Figure 3. (a) and (b) Calculations of the electronic band structure in nonmagnetic (NM) and antiferromagnetic (AFM) phases, respectively. (c) DFT calculations of  $\sigma_1(\omega)$  in the NM and AFM phases up to 2.5 eV. Inset shows a zoom-in view of the spectra below 0.6 eV.

citations and the AFM order. Figure 2(l) shows the temperature dependence of the absorption edge ( $\gamma$ ), extracted by linearly extrapolating the data to the horizontal axis. In general, the variation of the energy gap with  $T$  in semiconductors follows an empirical formula:  $E_g(T) = E_0 - aT^2/(T+b)$ , where  $E_0$  is the energy gap at 0 K, and  $a$  and  $b$  are constants [27]. Since the absorption edge provides an estimate of the energy gap, we apply this formula to fit the  $T$  dependence of the absorption edge. As shown by the red line in Figure 2(l), the position of the absorption edge deviates clearly from the expected behavior below 100 K. At the lowest measured temperature, the energy gap decreases by approximately 60 meV compared to the expected value. Note that this empirical formula is satisfied only when the temperature-dependent lattice dilation and electron-lattice interactions are considered. Therefore, the suppression of the energy gap at low temperatures is due to additional effects, like the interplay between the charge and spin degrees of freedom.

To figure out the impact of AFM order on the charge response, we performed DFT calculations of the electronic band structure in both nonmagnetic (NM) and AFM phases. In the NM phase, shown in Fig. 3(a), the energy gap between valence bands (VB1, VB2) and the conduction band (CB2) at the  $\Gamma$  point is approximately 0.3 eV. This gap corresponds to the absorption peak  $\beta$ , while the absorption edge around  $9000 \text{ cm}^{-1}$  is attributed to the interband transitions between VB3 and CB3. In the AFM phase, shown in Fig. 3(b), there is a band reconstruction caused by the band folding along  $k_z$  due to the unit cell doubling. The conduction band CB1 along the A-L direction folds to the  $\Gamma$ -M direction. Additionally, the Eu  $4f$  orbital forms flat bands located at around 1.5–2.0 eV below the Fermi level. The band repulsion between the Eu- $4f$  bands and the broad As bands shifts the occupied valence bands upward, reduc-

ing the gap at the  $\Gamma$  point, which gives rise to the emergence of peak  $\alpha$  at low temperatures. The band shift also leads to a decrease in the energy gap associated with the absorption edge  $\gamma$ . We also calculated the optical conductivity  $\sigma_1(\omega)$  in the NM and AFM phases. As shown in Fig. 3(c), the calculated  $\sigma_1(\omega)$  exhibits a prominent absorption peak near 2 eV (labeled as  $\delta$ ). Below this energy, the AFM  $\sigma_1(\omega)$  shows higher spectral weight due to new excitations arising from AFM-induced band folding, such as the interband transitions denoted as  $\Delta$  in Fig. 3. In the low-energy region, highlighted in the inset, the AFM calculations also show considerable excitations, as the energy gap is nearly closed in the AFM phase. These calculated results are consistent with our experimental observations.

Finally, we turn to the dynamics of the infrared-active

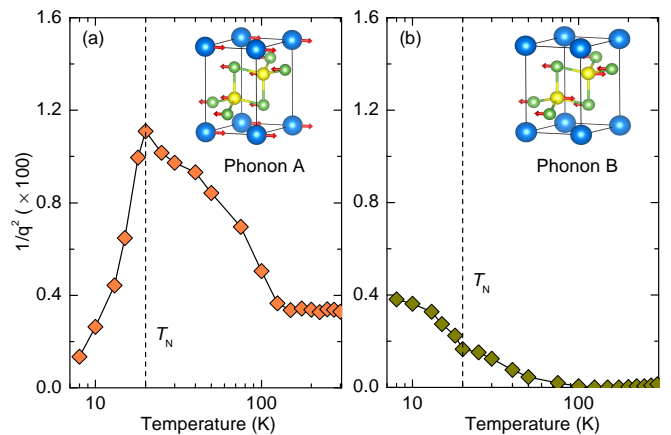


Figure 4. (a) and (b) Temperature dependence of the Fano parameter  $1/q^2$  for the infrared-active phonon modes at around 95 and 190  $\text{cm}^{-1}$ , respectively. The insets show displacement patterns of the phonon modes.

phonons in  $\text{EuZn}_2\text{As}_2$ . As shown in Fig. 2, both phonon modes exhibit asymmetric line shapes at low temperatures, which may result from coupling to either spins or charge excitations. To model these line shapes, the Fano oscillators are applied, and the obtained Fano parameters  $1/q^2$  are plotted in Fig. 4(a) for the  $95\text{ cm}^{-1}$  mode (phonon A) and Fig. 4(b) for the  $190\text{ cm}^{-1}$  mode (phonon B). Notably,  $1/q^2$  behaves differently across the AFM transition for these two modes. At high temperatures,  $1/q^2$  for both modes is either small or zero, indicating weak or no coupling. As the temperature decreases,  $1/q^2$  rises below 100 K, reflecting an enhancement in coupling strength. However, for phonon A,  $1/q^2$  drops suddenly below  $T_N = 20\text{ K}$ , while for phonon B,  $1/q^2$  continues to rise without any anomaly. Examining the atomic displacements of the phonon modes, we find that phonon A involves the vibrations of Eu atoms, while phonon B is dominated by the in-plane vibrations of Zn and As atoms. As a result, the lattice vibrations of phonon A are strongly coupled to the fluctuations of Eu spins. Below  $T_N$ , the spin-lattice coupling weakens due to the suppression of spin fluctuations. In contrast, phonon B, which does not involve Eu atoms, is unaffected by spin fluctuations. The asymmetric line shape of phonon B is primarily attributed to the coupling between phonon and charge excitations, which correlates with the enhancement of the  $\alpha$  peak below 100 K. Moreover, as detailed in the Supplemental Materials [26], other phonon parameters also show anomalies near  $T_N$ , reflecting the complex interplay of spin, lattice, and charge excitations in this system.

To summarize, magnetic order often induces significant changes in the electronic structure of magnetic topological materials [28–33], typically through exchange coupling between local spins and the *spd* electrons, leading to band splitting or shifts that can reduce or close the bulk band gap. In  $\text{EuZn}_2\text{As}_2$ , we observe a significant decrease in the band gap driven by the AFM order, but no nontrivial topological band inversion is detected. However, as discussed in the Supplemental Materials [26], a topological transition can be induced in this system by tuning the Hubbard  $U$ . Interestingly, a recent optical study of  $\text{EuCd}_2\text{As}_2$  [34] showed that applying a magnetic field induced a remarkable 15% reduction in the band gap. This suggests that a similar or even more pronounced change could occur in  $\text{EuZn}_2\text{As}_2$  under an external magnetic field or high pressure [24]. Therefore, these external factors may further modulate the interplay between spin, charge, and lattice degrees of freedom, giving rise to novel and fascinating electronic properties and possible topological phase transitions in  $\text{EuZn}_2\text{As}_2$ .

This work was supported by the National Key Research and Development Program of China (Grants No. 2024YFA1408301, No. 2022YFA1403900, No. 2023YFA1406002 and No. 2023YFF0718400), the National Natural Science Foundation of China (Grant No. 12274442) and the Guangdong basic and applied basic

research foundation (Grant No. 2023B151520013). P.M. and C.B. acknowledge funding by the Swiss National Science Foundation through Grants No. 200021-214905.

---

\* These authors contributed equally to this work.

† shenbing@mail.sysu.edu.cn

‡ hmweng@iphy.ac.cn

§ bingxu@iphy.ac.cn

- [1] B. Yan and C. Felser, Topological materials: Weyl semimetals, *Annu. Rev. Condens. Matter Phys.* **8**, 337 (2017).
- [2] B. A. Bernevig, C. Felser, and H. Beidenkopf, Progress and prospects in magnetic topological materials, *Nature* **603**, 41 (2022).
- [3] Y. Wang, F. Zhang, M. Zeng, H. Sun, Z. Hao, Y. Cai, H. Rong, C. Zhang, C. Liu, X. Ma, *et al.*, Intrinsic magnetic topological materials, *Front. Phys.* **18**, 21304 (2023).
- [4] X. Chen, S. Dong, and Z.-C. Wang, Recent advances in understanding and manipulating magnetic and electronic properties of  $\text{EuM}_2\text{X}_2$  ( $M=\text{Zn, Cd}$ ;  $X=\text{P, As}$ ), *J. Phys.: Condens. Matter* **37**, 033001 (2024).
- [5] J.-Z. Ma, S. Nie, C. Yi, J. Jandke, T. Shang, M.-Y. Yao, M. Naamneh, L. Yan, Y. Sun, A. Chikina, *et al.*, Spin fluctuation induced Weyl semimetal state in the paramagnetic phase of  $\text{EuCd}_2\text{As}_2$ , *Sci. Adv.* **5**, eaaw4718 (2019).
- [6] J.-R. Soh, F. De Juan, M. Vergniory, N. Schröter, M. Rahn, D. Yan, J. Jiang, M. Bristow, P. Reiss, J. Blandy, *et al.*, Ideal Weyl semimetal induced by magnetic exchange, *Phys. Rev. B* **100**, 201102 (2019).
- [7] L.-L. Wang, N. H. Jo, B. Kuthanazhi, Y. Wu, R. J. McQueeney, A. Kaminski, and P. C. Canfield, Single pair of Weyl fermions in the half-metallic semimetal  $\text{EuCd}_2\text{As}_2$ , *Phys. Rev. B* **99**, 245147 (2019).
- [8] J. Ma, H. Wang, S. Nie, C. Yi, Y. Xu, H. Li, J. Jandke, W. Wulfhekkel, Y. Huang, D. West, *et al.*, Emergence of Nontrivial Low-Energy Dirac Fermions in Antiferromagnetic  $\text{EuCd}_2\text{As}_2$ , *Adv. Mater.* **32**, 1907565 (2020).
- [9] K. Taddei, L. Yin, L. Sanjeeva, Y. Li, J. Xing, C. Dela Cruz, D. Phelan, A. Sefat, and D. Parker, Single pair of Weyl nodes in the spin-canted structure of  $\text{EuCd}_2\text{As}_2$ , *Phys. Rev. B* **105**, L140401 (2022).
- [10] Y. Xu, Z. Song, Z. Wang, H. Weng, and X. Dai, Higher-order topology of the axion insulator  $\text{EuIn}_2\text{As}_2$ , *Phys. Rev. Lett.* **122**, 256402 (2019).
- [11] H. Li, S.-Y. Gao, S.-F. Duan, Y.-F. Xu, K.-J. Zhu, S.-J. Tian, J.-C. Gao, W.-H. Fan, Z.-C. Rao, J.-R. Huang, *et al.*, Dirac surface states in intrinsic magnetic topological insulators  $\text{EuSn}_2\text{As}_2$  and  $\text{MnBi}_{2n}\text{Te}_{3n+1}$ , *Phys. Rev. X* **9**, 041039 (2019).
- [12] J. Jiang and S. M. Kauzlarich, Colossal magnetoresistance in a rare earth Zintl compound with a new structure type:  $\text{EuIn}_2\text{P}_2$ , *Chem. Mater.* **18**, 435 (2006).
- [13] Y. Zhang, K. Deng, X. Zhang, M. Wang, Y. Wang, C. Liu, J.-W. Mei, S. Kumar, E. F. Schwier, K. Shimada, C. Chen, and B. Shen, In-plane antiferromagnetic moments and magnetic polaron in the axion topological insulator candidate  $\text{EuIn}_2\text{As}_2$ , *Phys. Rev. B* **101**, 205126 (2020).

- [14] Z.-C. Wang, J. D. Rogers, X. Yao, R. Nichols, K. Atay, B. Xu, J. Franklin, I. Sochnikov, P. J. Ryan, D. Haskel, *et al.*, Colossal magnetoresistance without mixed valence in a layered phosphide crystal, *Adv. Mater.* **33**, 2005755 (2021).
- [15] J. Yan, Z. Z. Jiang, R. C. Xiao, W. Lu, W. Song, X. Zhu, X. Luo, Y. Sun, and M. Yamashita, Field-induced topological Hall effect in antiferromagnetic axion insulator candidate  $\text{EuIn}_2\text{As}_2$ , *Phys. Rev. Res.* **4**, 013163 (2022).
- [16] H. Li, W. Gao, Z. Chen, W. Chu, Y. Nie, S. Ma, Y. Han, M. Wu, T. Li, Q. Niu, *et al.*, Magnetic properties of the layered magnetic topological insulator  $\text{EuSn}_2\text{As}_2$ , *Phys. Rev. B* **104**, 054435 (2021).
- [17] F. Du, L. Yang, Z. Nie, N. Wu, Y. Li, S. Luo, Y. Chen, D. Su, M. Smidman, Y. Shi, *et al.*, Consecutive topological phase transitions and colossal magnetoresistance in a magnetic topological semimetal, *npj Quantum Mater.* **7**, 65 (2022).
- [18] H. Zhang, F. Du, X. Zheng, S. Luo, Y. Wu, H. Zheng, S. Cui, Z. Sun, Z. Liu, D. Shen, *et al.*, Electronic band reconstruction across the insulator-metal transition in colossally magnetoresistive  $\text{EuCd}_2\text{P}_2$ , *Phys. Rev. B* **108**, L241115 (2023).
- [19] S. Kreyber, M. Kopp, C. Garg, K. Kummer, J. Sichelschmidt, S. Schulz, G. Poelchen, M. Mende, A. V. Virovets, K. Warawa, *et al.*, Colossal magnetoresistance in  $\text{EuZn}_2\text{P}_2$  and its electronic and magnetic structure, *Phys. Rev. B* **108**, 045116 (2023).
- [20] Z.-C. Wang, E. Been, J. Gaudet, G. M. A. Alqasseri, K. Fruhling, X. Yao, U. Stuhr, Q. Zhu, Z. Ren, Y. Cui, *et al.*, Anisotropy of the magnetic and transport properties of  $\text{EuZn}_2\text{As}_2$ , *Phys. Rev. B* **105**, 165122 (2022).
- [21] J. Blawat, M. Marshall, J. Singleton, E. Feng, H. Cao, W. Xie, and R. Jin, Unusual electrical and magnetic properties in layered  $\text{EuZn}_2\text{As}_2$ , *Adv. Quantum Technol.* **5**, 2200012 (2022).
- [22] Z. Bukowski, D. Rybicki, M. Babij, J. Przewoźnik, L. Gondek, J. Żukrowski, and C. Kapusta, Canted antiferromagnetic order in  $\text{EuZn}_2\text{As}_2$  single crystals, *Sci. Rep.* **12**, 14718 (2022).
- [23] E. Yi, D. F. Zheng, F. Pan, H. Zhang, B. Wang, B. Chen, D. Wu, H. Liang, Z. X. Mei, H. Wu, *et al.*, Topological Hall effect driven by short-range magnetic order in  $\text{EuZn}_2\text{As}_2$ , *Phys. Rev. B* **107**, 035142 (2023).
- [24] S. Luo, Y. Xu, F. Du, L. Yang, Y. Chen, C. Cao, Y. Song, and H. Yuan, Colossal magnetoresistance and topological phase transition in  $\text{EuZn}_2\text{As}_2$ , *Phys. Rev. B* **108**, 205140 (2023).
- [25] J. Blawat, S. Speer, J. Singleton, W. Xie, and R. Jin, Quantum-limit phenomena and band structure in the magnetic topological semimetal  $\text{EuZn}_2\text{As}_2$ , *Commun. Phys.* **6**, 255 (2023).
- [26] See Supplemental Material at <http://link.aps.org/supplemental/xxx> for the details of sample synthesis, experimental methods, and DFT calculations.
- [27] Y. P. Varshni, Temperature dependence of the energy gap in semiconductors, *Physica* **34**, 149 (1967).
- [28] M. M. Otrokov, I. I. Klimovskikh, H. Bentmann, D. Estyunin, A. Zeugner, Z. S. Aliev, S. Gaß, A. Wolter, A. Koroleva, A. M. Shikin, *et al.*, Prediction and observation of an antiferromagnetic topological insulator, *Nature* **576**, 416 (2019).
- [29] C. Liu, Y. Wang, H. Li, Y. Wu, Y. Li, J. Li, K. He, Y. Xu, J. Zhang, and Y. Wang, Robust axion insulator and chern insulator phases in a two-dimensional antiferromagnetic topological insulator, *Nat. Mater.* **19**, 522 (2020).
- [30] Y. Deng, Y. Yu, M. Z. Shi, Z. Guo, Z. Xu, J. Wang, X. H. Chen, and Y. Zhang, Quantum anomalous Hall effect in intrinsic magnetic topological insulator  $\text{MnBi}_2\text{Te}_4$ , *Science* **367**, 895 (2020).
- [31] J. Li, Y. Li, S. Du, Z. Wang, B.-L. Gu, S.-C. Zhang, K. He, W. Duan, and Y. Xu, Intrinsic magnetic topological insulators in van der Waals layered  $\text{MnBi}_2\text{Te}_4$ -family materials, *Sci. Adv.* **5**, eaaw5685 (2019).
- [32] Q. Wang, Y. Xu, R. Lou, Z. Liu, M. Li, Y. Huang, D. Shen, H. Weng, S. Wang, and H. Lei, Large intrinsic anomalous Hall effect in half-metallic ferromagnet  $\text{Co}_3\text{Sn}_2\text{S}_2$  with magnetic Weyl fermions, *Nat. Commun.* **9**, 3681 (2018).
- [33] R. Yang, T. Zhang, L. Zhou, Y. Dai, Z. Liao, H. Weng, and X. Qiu, Magnetization-induced band shift in ferromagnetic Weyl semimetal  $\text{Co}_3\text{Sn}_2\text{S}_2$ , *Phys. Rev. Lett.* **124**, 077403 (2020).
- [34] D. Santos-Cottin, I. Mohelský, J. Wyzula, F. Le Mardelé, I. Kapon, S. Nasrallah, N. Barišić, I. Živković, J. Soh, F. Guo, *et al.*,  $\text{EuCd}_2\text{As}_2$ : A Magnetic Semiconductor, *Phys. Rev. Lett.* **131**, 186704 (2023).